

Complex-valued Convolutional Neural Network Enhanced Radar Imaging

Jingkun Gao, Bin Deng, Yuliang Qin, Hongqiang Wang and Xiang Li

Abstract—Convolutional neural networks (CNN) have been successfully employed to tackle several remote sensing tasks such as image classification and show better performance than previous techniques. For the radar imaging community, a natural question is: Can CNN be introduced to radar imaging and enhance its performance? The presented letter give an affirmative answer to this question. We firstly propose a processing framework by which CNN is used to enhance radar imaging. Then the core module of this framework, the complex-valued CNN (CCNN), is comprehensively derived. Special activation functions are also introduced to the proposed CCNN. Subsequently, the training-data-generation module is shown and some implementation details are presented. Finally, simulations and experiments are carried out. Both results show the superiority of the proposed method on imaging quality and efficiency.

Index Terms—Complex-valued convolutional neural network (CCNN), Convolutional neural network (CNN), Radar imaging, Super resolution, Side-lobe reduction

I. INTRODUCTION

IMPROVING radar imaging quality using signal processing techniques under given hardware platforms is an appealing topic and has attracted much attention [1],[2]. In the recent decade, compressive sensing [3] has fired an explosion on research of sparsity-driven radar imaging techniques [4],[5]. Typically, the following linear model is adopted

$$\mathbf{y} = \mathbf{A}\mathbf{x} + \mathbf{n}, \mathbf{y} \in \mathbb{C}^{M \times 1}, \mathbf{n} \in \mathbb{C}^{M \times 1}, \mathbf{x} \in \mathbb{C}^{N \times 1}, \mathbf{A} \in \mathbb{C}^{M \times N} \quad (1)$$

where \mathbf{y} is the echo signal, \mathbf{n} is the additive noise, \mathbf{x} represents the image to be estimated and \mathbf{A} is called the sensing matrix or the dictionary. According to (1), conventional imaging can be expressed as $\hat{\mathbf{x}} = \mathbf{A}^H \mathbf{y}$, which can be achieved by back projection (BP) or by Fast Fourier Transform (FFT) if certain conditions are met. However, either methods suffer from limited resolution, high side-lobes and strong speckles. Sparsity-driven methods impose prior constraints on \mathbf{x} and the imaging problem is transformed into an optimization problem

$$\hat{\mathbf{x}} = \arg \min_{\mathbf{x}} \psi(\mathbf{x}) \quad \text{s.t.} \quad \|\mathbf{y} - \mathbf{A}\mathbf{x}\|_2^2 < \sigma^2 \quad (2)$$

where $\psi(\mathbf{x})$ contains the prior knowledge on \mathbf{x} , σ^2 represents the energy of \mathbf{n} which is always unknown. The most widely used prior is the L1-norm constraint in the image domain, i.e. $\psi(\mathbf{x}) = \|\mathbf{x}\|_1$. The L1-norm constraint is also usually imposed to the transformed domain, i.e. $\psi(\mathbf{x}) = \|\mathbf{T}\mathbf{x}\|_1$,

where \mathbf{T} can be the wavelet transform, the derivation operator and so on. In addition, more complicated $\psi(\mathbf{x})$ s which take the inner coherence of \mathbf{x} into consideration are also proposed [6]. It can be expected that one can obtain better $\hat{\mathbf{x}}$ by designing more sophisticated $\psi(\mathbf{x})$ and developing more effective optimization algorithms.

Although sparsity-driven methods can improve imaging quality remarkably, it faces great challenges. Firstly, the time needs are usually too large for real time imaging. Different from linear imaging process, the optimization problem in (2) is nonlinear. Usually, a large amount of iterations are needed to converge to a reasonable solution, which makes them time consuming. Secondly, their stability and robustness are hardly guaranteed. The image enhancement obtained by solving (2) is based on accurate modeling. If \mathbf{A} is inaccurate or the constraint $\psi(\mathbf{x})$ is unsuitable, the results can be greatly degraded. Although several methods have been proposed for this problem [7], it is at the cost of heavier computational burden and the convergence still cannot be guaranteed.

In fact, the linear model in (1) and the regularization term in (2) is a general problem solving framework. In many other signal processing fields, e.g. image processing or computer vision [8], this methodology is also widely used. CNN is famous mostly for its cutting-edge performance in image classification tasks [9]. Recently, more and more researchers have extended and applied CNN to regression-type problems such as superresolution or denoising [10],[11]. In [10], the authors showed the close relationship between regression-type CNN and sparsity-based methods. In [12], the authors pointed out the similarity between the iterative solving process of sparsity-based methods and the feedforward process of CNN. Moreover, CNN can learn from and be adaptive to the training data, and its structure is highly parallel and free of iterations. As a result, CNN can outperform sparsity-based methods in both accuracy and efficiency.

On top of the above review, a reasonable question is whether CNN can be applied to radar imaging. In our opinion, applying CNN to radar imaging tasks needs several issues to be addressed. Firstly, what is the overall processing framework? e.g. what is the input and output of the CNN? Secondly, how can CNN handle radar echoes which are usually complex-valued numbers? Thirdly, how can we obtain the training data? Finally, is CNN more effective than sparsity-driven methods? In the following sections, we will introduce our solutions to these issues one by one.

II. METHODS

A. Overall framework of CCNN-enhanced radar imaging

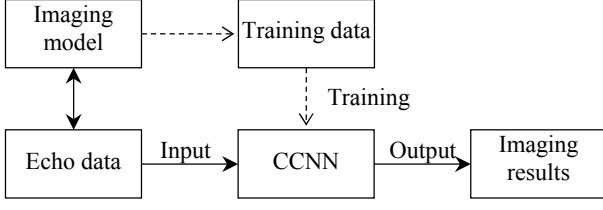


Fig. 1. Framework of CCNN-enhanced radar imaging

In Fig. 1, the dashed and solid lines show the data flow in training and imaging/testing period respectively. The imaging model contains all configurations and parameters that imaging needs. It can be seen that both training and imaging phases rely on the imaging model. Therefore, the premise of CCNN-enhanced radar imaging is to confirm the imaging model. Detailed discussions on CCNN and training data generation will be given in the following two sections.

B. The complex-valued convolutional neural network

We have noticed that there were articles talking about the CCNN in 1990s [13]. However, it did not attract much attention and relative research on this topic was suspended. More recently, some publications rediscovered CCNN and recognized some of its advantages [14],[15]. In fact, a complex number is just a couple of ordered real numbers and their calculations must comply with the rules defined by the imaginary unit j . From this point of view, we firstly present a much more comprehensive derivation of CCNN.

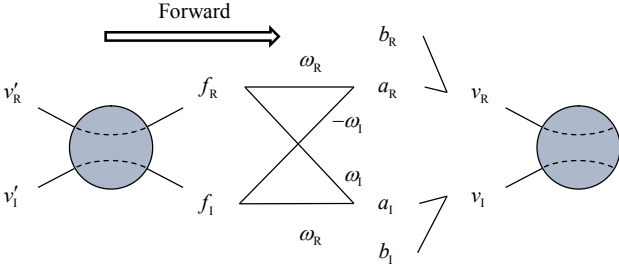


Fig. 2. Neuron and basic connection in CCNN

In Fig. 2, v' and v are the input of the neurons at lower and higher level respectively, f is the output of the neuron, ω is the weight, b is the bias, and $v', f, \omega, a, b, v \in \mathbb{C}$. Subscript “R” and “I” represent the real and imaginary parts respectively. Different from real-valued CNN (RCNN), the neuron of CCNN is of four “antennas”. The two on the left represent inputs while the right are outputs, and the dashed connections within the neuron are nonlinear transformations. One can note that the nonlinear transformations are applied to the real and imaginary parts independently. The connection is represented by the “butterfly” between the two neurons.

Suppose the cost function of CCNN is $E \in \mathbb{R}$ which will be defined latter. The key of network training is to solve the gradients of ω, b in each layer w.r.t. E . The following derivation takes the weight ω as an example. According to Fig. 2, the gradients of the real and imaginary parts are

$$\begin{cases} \partial E / \partial \omega_R = \partial E / \partial v_R \cdot \partial v_R / \partial \omega_R + \partial E / \partial v_I \cdot \partial v_I / \partial \omega_R \\ \partial E / \partial \omega_I = \partial E / \partial v_R \cdot \partial v_R / \partial \omega_I + \partial E / \partial v_I \cdot \partial v_I / \partial \omega_I \end{cases} \quad (3)$$

Based on complex-valued multiplication, one can obtain

$$\begin{cases} a_R = f_R \omega_R - f_I \omega_I \\ a_I = f_R \omega_I + f_I \omega_R \end{cases} \quad (4)$$

According to (4) and Fig. 2, it is easy to get

$$\begin{cases} \partial v_R / \partial \omega_R = f_R \\ \partial v_R / \partial \omega_I = -f_I \end{cases}, \begin{cases} \partial v_I / \partial \omega_R = f_I \\ \partial v_I / \partial \omega_I = f_R \end{cases} \quad (5)$$

$$\begin{cases} \partial v_R / \partial f_R = \omega_R \\ \partial v_R / \partial f_I = -\omega_I \end{cases}, \begin{cases} \partial v_I / \partial f_R = \omega_I \\ \partial v_I / \partial f_I = \omega_R \end{cases} \quad (6)$$

Based on the back propagation principles, we need to derive the recursive expression by which the lower layers' error term $\partial E / \partial v'_R, \partial E / \partial v'_I$ can be inferred by the higher layers' $\partial E / \partial v_R, \partial E / \partial v_I$. According to (6) and Fig. 2, we can get

$$\begin{cases} \frac{\partial E}{\partial v'_R} = \frac{\partial E}{\partial v_R} \frac{\partial v_R}{\partial f_R} \frac{\partial f_R}{\partial v'_R} + \frac{\partial E}{\partial v_I} \frac{\partial v_I}{\partial f_R} \frac{\partial f_R}{\partial v'_R} \\ \quad = (\partial E / \partial v_R \cdot \omega_R + \partial E / \partial v_I \cdot \omega_I) \cdot \partial f_R / \partial v'_R \\ \frac{\partial E}{\partial v'_I} = \frac{\partial E}{\partial v_R} \frac{\partial v_R}{\partial f_I} \frac{\partial f_I}{\partial v'_I} + \frac{\partial E}{\partial v_I} \frac{\partial v_I}{\partial f_I} \frac{\partial f_I}{\partial v'_I} \\ \quad = (-\partial E / \partial v_R \cdot \omega_I + \partial E / \partial v_I \cdot \omega_R) \cdot \partial f_I / \partial v'_I \end{cases} \quad (7)$$

Then (3) can be calculated using (5) and (7). $\partial E / \partial b_R$, $\partial E / \partial b_I$ can be solved similarly as $\partial v_R / \partial b_R = \partial v_I / \partial b_I = 1$.

The derivation above is a general procedure that makes up the basic building block of complex-valued neural networks. According to these basic formulas, we can train CCNN, complex-valued multi-layer perceptron (MLP) or more general complex-valued directed acyclic graphs (DAG) networks.

For the activation functions of CCNN, since they are applied to the real and imaginary parts independently, typical activation functions such as ReLU, Sigmoid or Tanh can be easily extended to CCNN. We use the complex-valued ReLU (cReLU) function defined as follow

$$f = \text{cReLU}(v') = \max(v'_R, 0) + j \max(v'_I, 0) \quad (8)$$

Differently, the activation function of the output layer is specifically defined as shown in Fig. 3.

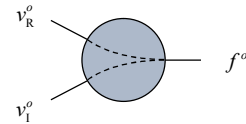


Fig. 3. Structure of the output layer neuron

The output layer activation function is defined as

$$f^o = |v_R^o + jv_I^o| = \sqrt{(v_R^o)^2 + (v_I^o)^2} \quad (9)$$

where superscript “o” indicates the output layer, and $f^o \in \mathbb{R}$. We can call this function as “Abs”. Then the definition of cost function can be given

$$E = \frac{1}{2} \sum (O - f^o)^2 \quad (10)$$

where $\sum \cdot$ is applied to all the output layer neurons, $O \in \mathbb{R}$ is the target function. The error term of the output layer are

$$\partial f^o / \partial v_R^o = v_R^o / f^o, \partial f^o / \partial v_I^o = v_I^o / f^o \quad (11)$$

According to (10), (11), (3) and (7), the gradient information can be back propagated to the parameters in all layers.

C. Generation of the training data

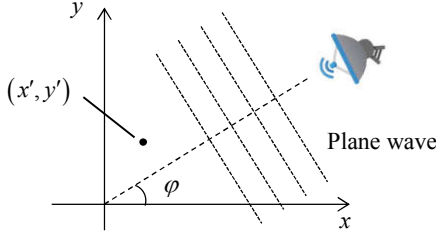


Fig. 4. Turntable imaging model

In this letter, we adopt the classical turntable model shown in Fig. 4. We can also learn from Fig. 1 that the input and output of the CCNN are radar echoes and expected images respectively. For real targets, the echo signals are determined by electromagnetic scattering equation

$$\mathbf{E}^s(\mathbf{r}) = \frac{jk \exp(jkR_0)}{4\pi R_0} \hat{k}_s \times \int_S \left(\hat{n} \times \mathbf{E}(\mathbf{r}') - \eta_0 \hat{k}_s \times (\hat{n} \times \mathbf{H}(\mathbf{r}')) \right) \exp(-jk(\hat{k}_s - \hat{k}_i) \cdot \mathbf{r}') d\mathbf{r}' \quad (12)$$

where $\mathbf{E}^s, \mathbf{E}, \mathbf{H}$ represent scattered wave, the total electric and magnetic fields on target's surface respectively. k is the wavenumber, R_0 is the distance from target to the observation point, \hat{k}_s, \hat{k}_i are the unit vectors of the scattering and incidence direction, S stands for the target's surface, \hat{n} is the unit normal, η_0 is the wave impedance. The echo signal is a complicated function of observation angle, polarization, frequency, and there is no explicit expression of the expected target function. To train CCNN, input and output must be exactly defined. Consequently, necessary simplification is applied to (12). Concretely, the ideal point scattering model is used and the scattering is confined within 2D spaces. Neglecting the attenuation and the propagation phase term, we can obtain the echo under turntable model as

$$E^s(k, \varphi) = \sum_{x', y'} o(x', y') \cdot \exp(-2jk(x \cos \varphi + y \sin \varphi)) \quad (13)$$

where $o(x', y') \in \mathbb{C}$ represents the target's scattering coefficients. Then we can explicitly defined the expected target function as

$$O(x, y) = p(x, y) * |o(x, y)| \quad (14)$$

where $*$ stands for convolution, $O(x, y) \in \mathbb{R}$ is the same function in (10) and $p(x, y)$ is the ideal point spread function (PSF). We define $p(x, y)$ as

$$p(x, y) = \exp(-x^2/\sigma_x^2 - y^2/\sigma_y^2) \quad (15)$$

where σ_x, σ_y control the width of $p(x, y)$. According to the

-3 dB definition, we can deduce the resolution in these two directions are $1.18\sigma_x, 1.18\sigma_y$ respectively.

III. RESULTS

A. Network structure and implementation details

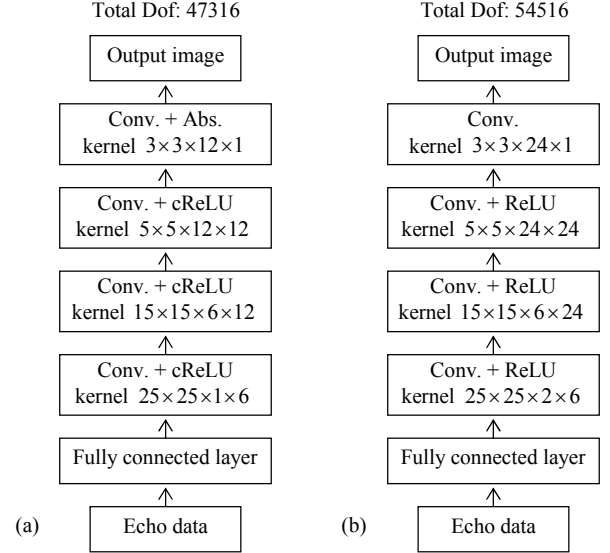


Fig. 5. Network structures of (a) proposed CCNN and (b) counterpart RCNN

Recently, the fully connected layer in the network is achieved by $\hat{\mathbf{x}} = \mathbf{A}^H \mathbf{y}$. For large scale problems, the number of elements in \mathbf{A} can approach the order of 10^9 . Therefore, FFT is employed to realize $\hat{\mathbf{x}} = \mathbf{A}^H \mathbf{y}$ fast and implicitly. As a result, the weights of the fully connected layer do not exist explicitly, and they are also excluded in the training phase. For comparison, a similar RCNN is also designed. The real and imaginary parts of the data are treated as two independent channels. The total degree of freedom (Dof) of the RCNN is designed to be higher than that of the CCNN.

For training data generation, we first randomly generate hundreds of coordinates (x', y') within a squared area using uniform distribution. Then scattering coefficients are generated using standard complex Gaussian distribution, i.e. $o(x', y') \sim N(0, 1) + jN(0, 1)$. Training data at the input and output ports are obtained by (13) and (14) respectively.

Momentum stochastic gradient descent is used and the momentum is 0.9. Weight decay technique is also employed and the coefficient is 0.001. The learning rate is 3×10^{-5} for the first three layers, and 1×10^{-5} for the last layer. The batch size is 50, and 50000 examples are generated for training. Training lasts for 5 epochs. Our recent implementation is based on MATLAB and CUDA. A NVIDIA TITAN Xp card is used, and the training takes approximately 16 hours.

For sparsity-driven imaging, we take SPGL1 [16] as a representative to compete with the proposed method. There are three reasons that make SPGL1 a good choice. 1) It supports implicit implementation of \mathbf{A} . For large scale problems, explicit \mathbf{A} will lead to unacceptable memory cost and block the computation. 2) It is compatible with complex-valued

problems. Complex-valued data must be transformed to real ones to comply with real-valued algorithms. This doubles the size of the matrices and vectors, or it sometimes may lead to a wrong solution. 3) High executive efficiency. We have tested several algorithms and found that SPGL1 is relatively fast especially for large scale problems.

B. Numerical simulations

TABLE I
IMAGING PARAMETERS

Probing frequency	213.6 GHz ~ 226.4 GHz
Rotation angle ϕ	-1.68°~1.67°
Number of frequency samplings	500
Number of angle samplings	300
Region of imaging	0.7×0.7 m ²
Number of pixels in the image	236×236
σ_x, σ_y	0.4 cm

From Table 1, it is easy to calculate that the range and azimuth resolutions are 1.17 cm and 1.15 cm respectively. Both σ_x, σ_y are set to be 0.4 cm which suggests a 0.47 cm resolution, and the expected superresolution ratio is about 2.5. According to [17], the rotation angle is relatively small, and imaging can be done by 2D IFFT. In fact, the linear operator \mathcal{A} and \mathcal{A}^H in this letter are implicitly implemented by 2D IFFT and 2D FFT. It should be claimed that these fast implementations introduce some errors into \mathcal{A} and \mathcal{A}^H since FFT-based imaging actually approximates the fan-shaped spectral domain support area into a rectangular one. Fig. 6 shows the imaging results of the “NUDT” made up of several unit ideal point scatters. The groundtruth image generated by (14) is also shown in Fig. 6.

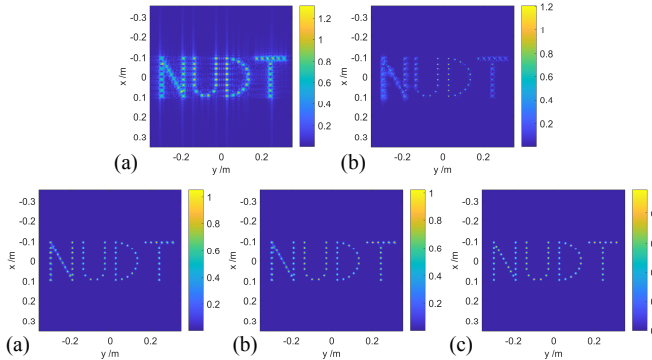


Fig. 6. Imaging results of “NUDT” by (a) FFT (b) SPGL1 (c) RCNN (d) CCNN, and (e) groundtruth image

In Fig. 6(a), we can see that the image is of high side-lobes and relatively low resolution. We notice that the points located around the center are focused better than those close to the borders. In [18], this phenomenon is carefully analyzed, and it is caused by the errors introduced into \mathcal{A} we mentioned above. In Fig. 6(b), similar phenomenon can also be observed since the errors in \mathcal{A} impact the solving of SPGL1. Compared with Fig. 6(a) and (b), (c) and (d) achieve higher quality visually, and they are also more similar to the groundtruth image in (e). For RCNN and CCNN, their recent fully connected layers are implicitly implemented by 2D IFFT. However, the networks can automatically fix these errors in \mathcal{A}^H since the following convolutional layers are adaptive. As a result, RCNN and CCNN are more robust to modeling errors. Quantitatively, the

root mean square error (RMSE) is calculated as performance index. The RMSEs of different methods under different SNRs are listed in Table 2. For each SNR level and each method, RMSE is the average of 100 times experiments’ results. The testing data are generated in the same way with the training data. The time needs of different methods are the mean value of all the experiments for each method.

TABLE II

COMPARISON ON RMSES AND TIME NEEDS FOR DIFFERENT METHODS

Methods	RMSE, -10dB	RMSE, -5dB	RMSE, 0dB	RMSE, 5dB	RMSE, 10dB	Time needs
FFT	0.1987	0.1778	0.1705	0.1682	0.1675	0.042 s
SPGL1	0.0568	0.0560	0.0568	0.0574	0.0683	27.66 s
RCNN	0.0456	0.0308	0.0262	0.0251	0.0248	0.083 s
CCNN	0.0434	0.0289	0.0255	0.0247	0.0245	0.071 s

For all SNR levels, CCNN performs the best. For time needs, CCNN is closely after the FFT-based method. As the fully connected layer of CCNN is achieved by FFT and its time need can no way better than FFT-based method recently. Compared with SPGL1, the imaging process of CCNN is just the feedforward process of the network which can be easily parallelized and greatly accelerated by GPU. Therefore, CCNN costs much less time than SPGL1 and can meet the requirements for most real time imaging scenarios. While using SPGL1 for imaging, the SNR is imported into the algorithm as a known parameter which is not always the case for real applications. Moreover, it can be seen that the RMSEs of SPGL1 is not monotonic with the increasing of SNR. We think this is mainly caused by two reasons. 1) The algorithm is not quite stable since errors exist in \mathcal{A} . 2) The groundtruth produced by (15) does not encourage image’s sparsity too much. For RCNN, its performance is weaker than CCNN although there are 7200 more parameters. We think this is because the structure shown in Fig. 2 is essentially more efficient for modeling complex-valued problems.

C. Laboratory results

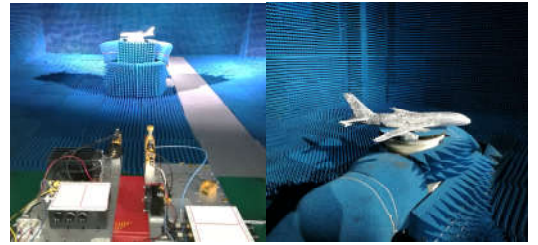


Fig. 7. Experiment scenario

The experiment scenario is shown in Fig. 7 and an airplane model is used as the target. Other imaging parameters are the same with those listed in Table 1.

In Fig. 8, images are displayed in log-magnitude and the dynamic range is 35 dB. The time needs are similar with those listed in Table 2 since imaging parameters are the same. Unsurprisingly, the resolution of FFT-based image is relatively low while the side-lobes are extremely high. All other methods enhance the resolution and suppress the side-lobes while their visual impression differ from each other apparently. Since it is hard to define groundtruth for real targets, quantitative comparisons on image quality are not conducted. Moreover, the quality assessment of radar images is still an open question.

Nevertheless, recent results have shown the superiority of the proposed method on robustness and efficiency.

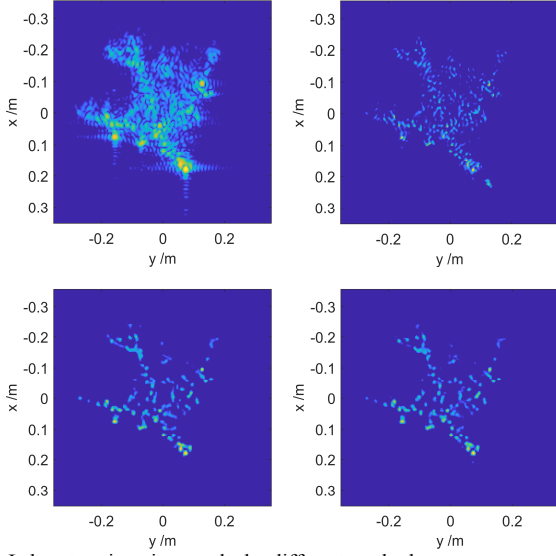


Fig. 8. Laboratory imaging results by different methods

In addition, we think our work is only the first step of CCNN-enhanced radar imaging and it can be further improved in several aspects. The proposed CCNN is trained under ideal point scattering assumption. This indicates that current CCNN is actually point-feature-enhancement oriented. By using more realistic scattering models, enhancement of more potential features of the target can be expected. Also, in recent work, all needed imaging parameters are known. In real applications, due to the uncertainty of movements, some parameters must be estimated. Whether CCNN can be designed or trained to achieve automatic focusing is also an appealing question.

IV. CONCLUSION

A novel CCNN-enhanced radar imaging method is proposed. A processing framework is firstly presented. Comprehensive definitions of the complex-valued neurons and connections in CCNN are given, and the basic building block of complex-valued back propagation is derived. The cReLU activation function is proposed and used. For the neurons in the output layer, the “Abs” activation function is used. Then our method of generating training data for the CCNN is introduced. Different from iterative-based imaging methods, the imaging process of CCNN is just the feedforward process of the network. This makes CCNN much faster and makes it possible to achieve enhanced real time imaging. CCNN-based method is also more robust since it is adaptive to the training data. Compared with its real-valued counterpart, CCNN achieves better performance with less parameters. Finally, we present several interesting future directions, and we believe CCNN will

bring more benefits to radar imaging in the future.

REFERENCES

- [1] L. Zhao, L. Wang, L. Yang, A. M. Zoubir and G. Bi, "The Race to Improve Radar Imagery: An overview of recent progress in statistical sparsity-based techniques," *IEEE Signal Processing Magazine*, vol.33, no.6, pp. 85-102, 2016.
- [2] S. Zhang, Y. Liu and X. Li, "Autofocusing for Sparse Aperture ISAR Imaging Based on Joint Constraint of Sparsity and Minimum Entropy," *IEEE Journal of Selected Topics in Applied Earth Observations & Remote Sensing*, vol.10, no.3, pp. 998-1011, 2017.
- [3] D. L. Donoho, "Compressed sensing," *IEEE Transactions on Information Theory*, vol.52, no.4, pp. 1289-1306, 2006.
- [4] G. Xu, M. Xing, L. Zhang, Y. Liu and Y. Li, "Bayesian Inverse Synthetic Aperture Radar Imaging," *IEEE Geoscience & Remote Sensing Letters*, vol.8, no.6, pp. 1150-1154, 2011.
- [5] M. Cetin, I. Stojanovic, O. Onhon and K. Varshney, "Sparsity-Driven Synthetic Aperture Radar Imaging: Reconstruction, autofocusing, moving targets, and compressed sensing," *IEEE Signal Processing Magazine*, vol.31, no.4, pp. 27-40, 2014.
- [6] L. Wang, L. Zhao, G. Bi and C. Wan, "Sparse Representation-Based ISAR Imaging Using Markov Random Fields," *IEEE Journal of Selected Topics in Applied Earth Observations & Remote Sensing*, vol.8, no.8, pp. 3941-3953, 2015.
- [7] X. Zhou, H. Wang, Y. Cheng and Y. Qin, "Off-Grid Radar Coincidence Imaging Based on Variational Sparse Bayesian Learning," *Mathematical Problems in Engineering*, vol.2016, pp. 1-12, 2016.
- [8] M. Elad, M. A. T. Figueiredo and Y. Ma, "On the Role of Sparse and Redundant Representations in Image Processing," *Proceedings of the IEEE*, vol.98, no.6, pp. 972-982, 2010.
- [9] A. Krizhevsky, I. Sutskever and G. E. Hinton, "ImageNet classification with deep convolutional neural networks," *Communications of the Acm*, vol.60, no.2, pp. 2012, 2012.
- [10] C. Dong, C. L. Chen, K. He and X. Tang, "Image Super-Resolution Using Deep Convolutional Networks," *IEEE Transactions on Pattern Analysis & Machine Intelligence*, vol.38, no.2, pp. 295-307, 2016.
- [11] K. Zhang, W. Zuo, Y. Chen, D. Meng and L. Zhang, "Beyond a Gaussian Denoiser: Residual Learning of Deep CNN for Image Denoising," *IEEE Transactions on Image Processing*, vol.26, no.9, pp. 4509-4522, 2017.
- [12] K. H. Jin, M. T. Mccann, E. Froustey and M. Unser, "Deep Convolutional Neural Network for Inverse Problems in Imaging," *IEEE Transactions on Image Processing*, vol.26, no.9, pp. 4509-4522, 2017.
- [13] G. M. Georgiou and C. Koutsougeras, "Complex domain backpropagation," *IEEE Transactions on Circuits & Systems II Analog & Digital Signal Processing*, vol.39, no.5, pp. 330-334, 1992.
- [14] C. Trabelsi, O. Bilaniuk, Y. Zhang, D. Serdyuk, S. Subramanian and J. F. Santos, et al., "Deep Complex Networks," *arXiv preprint arXiv:1705.09792*, 2017.
- [15] Z. Zhang, H. Wang, F. Xu and Y. Q. Jin, "Complex-Valued Convolutional Neural Network and Its Application in Polarimetric SAR Image Classification," *IEEE Transactions on Geoscience & Remote Sensing*, vol.55, no.9, pp. 1-12, 2017.
- [16] V. D. B. Ewout and M. P. Friedlander, "Probing the Pareto Frontier for Basis Pursuit Solutions," *Siam Journal on Scientific Computing*, vol.31, no.2, pp. 890-912, 2008.
- [17] J. K. Gao, Y. L. Qin, B. Deng, H. Q. Wang, J. Li and X. Li, "Terahertz Wide-Angle Imaging and Analysis on Plane-wave Criteria Based on Inverse Synthetic Aperture Techniques," *Journal of Infrared Millimeter & Terahertz Waves*, vol.37, no.4, pp. 373-393, 2016.
- [18] J. K. Gao, Z. M. Cui, B. B. Cheng, Y. L. Qin, X. J. Deng and B. Deng, et al., "Fast Three-Dimensional Image Reconstruction of a Standoff Screening System in the Terahertz Regime," *IEEE Transactions on Terahertz Science & Technology*, vol.5, no.9, pp. 1-14, 2017.